A Novel Method for Snow Depth Retrieval Using Improved Dense Medium RVoG Model

Haiwei Qiao, Ping Zhang, Zhen Li, *Member, IEEE*, Lei Huang, *Member, IEEE*, Zhipeng Wu, Shuo Gao, Chang Liu, Shuang Liang, Jianmin Zhou, Wei Sun, and Jian Wang

***Abstract*—Snow depth is a fundamental parameter in hydrological and climate models, which is crucial for studying climate change, hydrological cycles, and ecosystem changes. Polarimetric synthetic aperture radar interferometry (PolInSAR) is one of the most promising snow depth retrieval methods, which is sensitive to the shape, direction, and vertical distribution of targets. The dense medium random-volume-over-ground (DM-RVoG) model for PolInSAR has been shown to be workable for snow depth retrieval, it still suffers from the inaccuracy of the parameters representing the phase center and decorrelation. In this study, based on the backscattering mechanism of snow, a novel snow depth retrieval method is proposed to improve the DM-RVoG model using polarization decomposition and decorrelation optimization. First, the polarization decomposition is extended to obtain the ground scattering phase. Then, the coherence region boundary estimation method is put forward to obtain pure volume decorrelation. Finally, the proposed method is validated using Ku-band UAV SAR data, and the accuracy is assessed using in situ data. The correlation coefficient, root mean square error, and mean absolute error of the proposed method are 0.88, 4.98, and 4.08 cm, respectively, demonstrating significant improvements compared with the original method.**

***Index Terms*—Improved dense medium random-volume-over-ground (RVoG) model, interferometry, Ku-band, polarimetric synthetic aperture radar interferometry (PolInSAR), snow depth, UAV synthetic aperture radar (SAR).**

I. Introduction

SNOW plays a key role in global change, and accurately monitoring snow and its parameters is a promising research direction [1], [2]. Snow depth (SD) is a crucial physical parameter for evaluating snow variation and affects the precision of climate and hydrological models, which is also important for predicting disasters [1], [3]. Traditionally, SD is monitored manually or by relying on meteorological stations, but obtaining large and continuous SD on the ground is still a challenging task due to the harsh terrain and weather conditions in snow-covered areas [4], [5]. Affected by these conditions and short wavelengths, it is also relatively difficult for optical remote sensing to obtain the internal characteristic parameters of snow such as SD [4]. Previously, microwave remote sensing has been extensively employed to estimate SD [6], [7], which can overcome not only harsh weather conditions, but also has a variety of high-frequency bands that effectively interact with snowpack to accurately retrieve SD [8], [9].

Synthetic aperture radar (SAR) remote sensing provides higher spatial resolution, which has more potential for finely retrieving SD [10]. Polarimetric SAR (PolSAR) utilizes multipolarization channel information for retrieving parameters, which is sensitive to the shape and direction of the target and it has a relatively mature application in retrieving SD [11], [12], [13]. One of the most common methods is the co-polar phase difference (CPD), which is used to express the phase difference of the signal delay between HH and VV polarization channels [9]. From this, relationships between parameters such as snow depth, interaxis ratio, and snow density are constructed for retrieving SD based on the propagation path of the two polarization channel signals within the snowpack [9], [13]. Snow backscatter modeling can also be used to retrieve snow parameters based on PolSAR [14], [15], [16]. In addition, the PolSAR decomposition method has been gradually used to retrieve SD with good results [11], [12].

Interferometric SAR (InSAR) is more responsive to the height structure of the target and is one of the promising methods for retrieving the target height introduced in recent years [17]. According to the different SAR data acquisition modes, InSAR can be classified into two types: single-pass InSAR and repeat-pass

Manuscript received 22 April 2023; revised 3 July 2023, 16 August 2023, and 5 November 2023; accepted 6 December 2023. Date of publication 14 December 2023; date of current version 28 December 2023. This work was supported in part by the National Key Research and Development Program of China under Grant 2018YFA0605403, in part by the International Partnership Program of the Chinese Academy of Sciences under Grant 131C11KYSB20160061, in part by the Key Deployment Program of AIRCAS under Grant Y950930Z2F, and in part by the National Natural Science Foundation of China under Grant 41971393 and Grant 42071084. *(Corresponding author: Ping Zhang.)*

Haiwei Qiao is with the Key of Digital Earth Science, Aerospace Information Research Institute, Chinese Academy of Sciences, Beijing 100094, China, also with the International Research Center of Big Data for Sustainable Development Goals, Beijing 100094, China, and also with the University of Chinese Academy of Sciences, Beijing 100049, China (e-mail: qiaohaiwei20@mails.ucas.edu.cn).

Ping Zhang, Zhen Li, Lei Huang, Zhipeng Wu, Chang Liu, Shuang Liang, and Jianmin Zhou are with the Key Laboratory of Digital Earth Science, Aerospace Information Research Institute, Chinese Academy of Sciences, Beijing 100094, China, and also with the International Research Center of Big Data for Sustainable Development Goals, Beijing 100094, China (e-mail: zhangping@aircas.ac.cn; lizhen@aircas.ac.cn; huanglei@radi.ac.cn; wuzhipeng19@mails.ucas.ac.cn; liuc5@radi.ac.cn; liangpr@radi.ac.cn; zhoujm@aircas.ac.cn).

Shuo Gao is with the National Engineering Laboratory for Satellite Remote Sensing Applications, Aerospace Information Research Institute, Chinese Academy of Sciences, Beijing 100094, China (e-mail: gaoshuo@radi.ac.cn).

Wei Sun is with the Aerospace Information Research Institute, Chinese Academy of Sciences, Beijing 100094, China (e-mail: sunwei001890@aircas.ac.cn).

Jian Wang is with the School of Spatial Informatics and Geomatics Engineering, Anhui University of Science and Technology, Huainan 230001, China (e-mail: wangjianhsy@outlook.com).

Digital Object Identifier 10.1109/JSTARS.2023.3342993

InSAR [18]. Single-pass InSAR is almost free from temporal decorrelation and atmospheric delay effects, and the phases from the two antennae can be used directly to indicate the wet snow depth of the top layer [19]. However, for dry snow mixed with ground/volume scattering, snow depth retrieval based on single-pass InSAR needs to be combined with the InSAR model and consider the applicability of the spatial baseline to the model, which increases the complexity of the snow depth retrieval method for dry snow from the single-pass InSAR data [18]. The repeated-pass InSAR uses the phase of SAR data before and after snowfall to retrieve snow depth, which may suffer from temporal decorrelation, but the repeated-pass InSAR can obtain the phase difference information from before and after snowfall easily, which is the wider application in dry snow depth retrieval [18]. In addition, many studies have retrieved SD using differential interferometric synthetic aperture radar (D-InSAR) methods [20], [21]. For instance, the D-InSAR phases in the VV and VH polarization were corrected using snow-cover images, and this approach can obtain relatively accurate SD retrieval results [22].

However, the above snow depth retrieval methods based on PolSAR and InSAR still have some problems. The PolSAR-based snow depth retrieval methods are affected by the lack of target vertical information in the two-dimensional SAR images, and almost all of them need to establish some empirical relationships to retrieve the snow depth. For example, the CPD snow depth retrieval method needs to construct the empirical relationship between the measured snow depth and the co-polarization phase difference, and the polarization decomposition-based snow depth retrieval method needs to construct the empirical relationship between the measured snow depth and the backscattering coefficient. These empirical relationships depend on in situ data, thus they will be different in different regions, which results in the poor generalizability of the PolSAR-based snow depth retrieval methods. The traditional InSAR-based snow depth retrieval method utilizes the phase information of two SAR images to effectively extract the vertical information of the target. However, it lacks the backscattering information of the snow, which makes it impossible to distinguish multiple scattering mechanisms in the vertical direction from the same resolution unit and increases the uncertainty of snow depth retrieval.

Polarization synthetic aperture radar interferometry (PolInSAR) combines the advantages of PolSAR in identifying different scattering mechanisms and the advantage of InSAR in determining the location of the scattering center, which is a very promising method for retrieving the vertical information from targets [23]. In past studies, PolInSAR has been widely used in forest height retrieval and glacier dynamic monitoring [23], [24], [25]. However, compared with forests and glaciers, snow has a smaller thickness and is a dense medium, thus traditional retrieval methods for PolInSAR cannot be directly applied. In recent years, some studies have tried to use PolInSAR to retrieve SD and proved that PolInSAR has great potential in retrieving SD, for example, semi-empirical model [26], CAI model [4], hybrid DEM differencing and coherence amplitude algorithm [27], and dense medium random-volume-over-ground (DM-RVoG) model [18]. Among them, the recently proposed DM-RVoG model involving the dense medium properties of snow is very attractive for retrieving SD. The basis of the DM-RVoG model for retrieving SD is to accurately extract the ground scattering phase center (φ_{g}) and the pure volume correlation ($\gamma_{\mathrm{vol\_op}}$). However, the original method has some problems when extracting these parameters, for example, the original method is improper when using the fitting method to directly obtain the ground phase and assuming that the HV polarization does not contain ground scattering. To address the above shortcomings, we propose to improve the parameter extracting method in the DM-RVoG model by using the polarization decomposition method and coherence region boundary estimation method to improve the performance of SD retrieval. The precision of the suggested method is evaluated and discussed using Ku-band SAR data and measured data obtained in Altay.

The rest of this article is organized as follows. Section II introduces the study area and data. In Section III, the types of backscattering from snow and the novel method are presented. In Section IV, the SD retrieval results and the accuracy assessment results of the novel method are presented. In Section V, the factors affecting the performance of the novel method are discussed. In Section VI, a summary of the novel method is provided and potential developments are suggested.

II. Study Area and Data

A. Study Area

The study area is the Altay region, one of the typical snow-covered areas in China, and the specific location is in the west of the Altay region. The study area has prolonged cold winters, averaging –10 °C in March, with even colder temperatures in the first half of March [28]. The study area has a small altitude difference of only 22 m. The snow in this area is seasonal, with an average snow depth of about 20 cm during the experiment in early March. The underlying surface type of snow is Gobi [28]. Fig. 1 shows the study area on a map with the Google Earth image in the background.

B. UAV-SAR Data Acquisition, Evaluation, and Preprocessing

1) UAV-SAR Data Acquisition: The flight data of the study area were acquired using Ku-band SAR sensors mounted on the UAV [29]. The SAR data were acquired on March 8, 2021. While collecting SAR data, a repeat-pass (two flights) with a 21.35 m spatial baseline was conducted to satisfy the requirements of the DM-RVoG model. Considering the possibility of temporal decorrelation, the imaging time of the SAR image pair was within 0.5 h. The time used for one flight was about 15 min. Table I shows the primary parameters of the UAV SAR. It contains four polarization modes with a wavelength of 0.0203 m.

2) UAV-SAR Data Evaluation: Before acquiring the SAR data, we set up five artificial angle reflectors (CRs) in the study area for evaluating and correcting the SAR data. The positions of the CRs are denoted with yellow pins in Fig. 1, and the actual placement is exhibited in Fig. 2(a). Fig. 2(b) and (c) display the response functions of one of the CRs. We

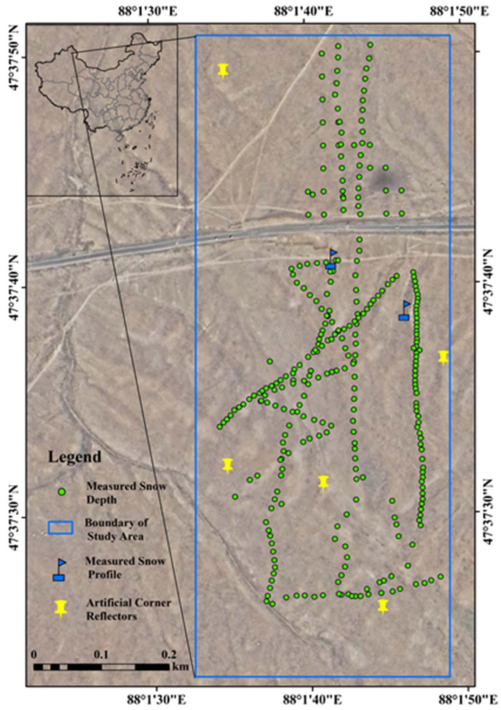

Fig. 1. Study area and the in situ measurement points in the field. The blue square is the flight area. The green points are in situ SD points. The yellow pins denote the locations of the corner reflectors. The flag is snow profile. The background image is from Google Earth.

TABLE I
MAIN PARAMETERS OF AIRCAS SAR DATA

Sensor Name	IECAS
Bandwidth	1.2 GHz
Freq. band	Ku
Wavelength	0.0203 m
Range Resolution	0.16 m
Azimuth Resolution	0.1 m
Polarization	HH, HV, VH, VV

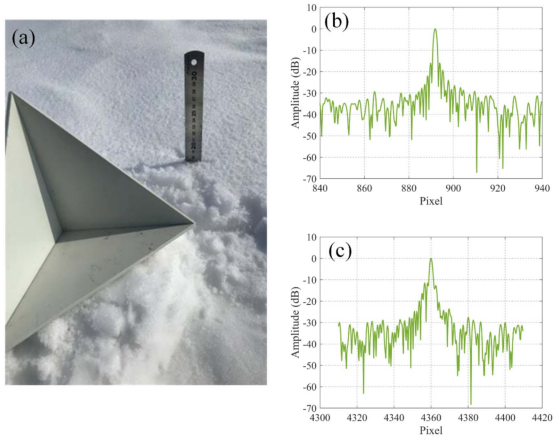

Fig. 2. Placement and response function of corner reflectors. (a) Is the CR. (b) and (c) are the response functions of one CR in the range and azimuth direction.

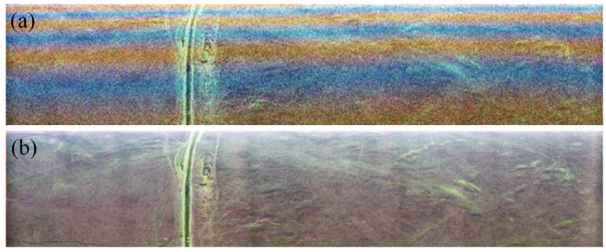

Fig. 3. Pauli images before and after polarization calibration. (a) Is the Pauli image before polarization calibration. (b) Is the Pauli image after polarization calibration.

chose peak side lobe ratio (PSLR) and integrated side lobe ratio (ISLR) to evaluate the SAR image performance, where PSLR was –15.79 and –9.90 dB in azimuth-range direction without windowed, respectively. ISLR was –13.62 and –8.6 dB in the range-azimuth direction without windowed, respectively. This indicates that SAR images exhibited good performance for the application. In addition, we found significant streaks in the Pauli image as shown in Fig. 3(a), for which we corrected the bias in the data by polarization calibration. The calibration process mainly has three parts, including phase calibration, polarization channel crosstalk calibration, and channel imbalance parameter calibration. The corrected Pauli image is shown in Fig. 3(b), with the interchannel error eliminated.

3) Preprocessing UAV-SAR Data: Registration of SAR data: SAR pairs need to be registered before interferometric processing. To register the two images, a coarse registration method and a fine registration method were used in this study [30]. The disparity between two images following registration was under one pixel.

Elimination of flat earth effects: Because of flat terrain, the interference phase varied periodically. Although the phenomenon was not obvious in the airborne SAR data, the flat earth effects cannot be ignored, and we used the fringe frequency method to eliminate the flat earth effects [31].

Geocoding: Geocoding is converting the SAR images to a geographic coordinate system, which is a necessary step to correspond to the in situ data for subsequent accuracy assessment. The reverse-range-doppler method was applied for geocoding [32].

C. Field Measurement

The study area is small and the number of meteorological stations is insufficient, therefore, some SD points were measured in this study to assess the proposed method. SD measurements were randomly and uniformly distributed in the study area, as shown in Fig. 1. By analyzing the coherence of the SAR pairs, we utilized 80 observed SD points in the vicinity of the corner reflectors for the accuracy evaluation. The snow depths ranged from 4 to 50 cm with an average depth of approximately 20 cm, representing the typical snow conditions in the study area. Fig. 4 shows working photos of the SD measurement. We chose a suitable snow profile and used a straightedge to measure it and measured twice at the same time to prevent errors.

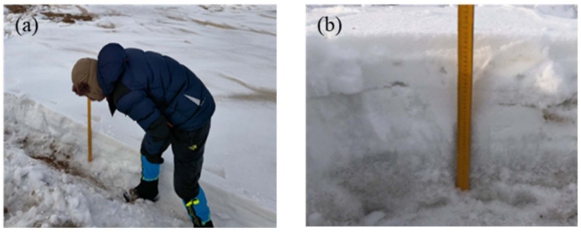

Fig. 4. In situ measurement scene. (a) Is the actual working scene. (b) Is a photo of the snow profile.

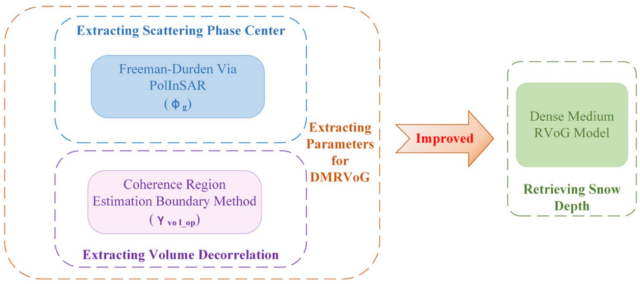

Fig. 5. Proposed method by improved DM-RVoG model. The polarization decomposition method and the coherence region estimation method are used to improve the DM-RVoG model.

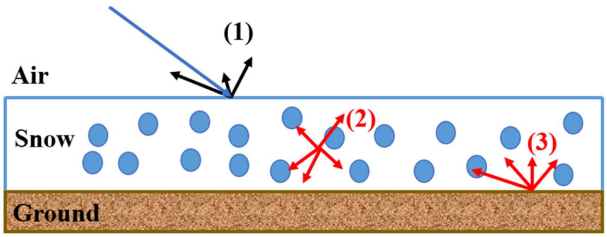

Fig. 6. Different components and types of backscattering from snow.

III. Methodology

In this section, the improved DM-RVoG model by optimizing the parameters representing the phase center and decorrelation is suggested to retrieve SD, as shown in Fig. 5. First, the components and types from snow backscattering are described as a basis. Then, improved methods for extracting parameters in the DM-RVoG model are described. In addition, the strategy of the DM-RVoG model for retrieving SD is introduced. At the same time, the implementation process of the novel method is described. Finally, accuracy metrics are introduced.

A. Backscattering From Snow

The scattering and attenuation process from snow is mainly determined by the sensor and target parameters. The sensor parameters include wavelength, incident angle, and antenna configuration. The target parameters include the geometric and dielectric properties of snow [33]. There are three backscattering components from snow, as shown in Fig. 6.

1) Surface scattering from the air-snow interface.
2) Volume scattering from the snowpack.
3) Surface scattering from the snow-ground interface [33].

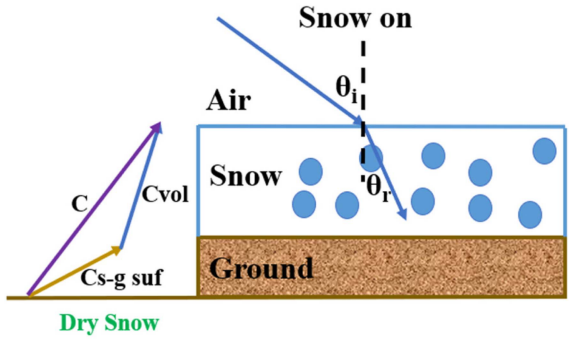

Fig. 7. Various scattering types from dry snow whose underlying surface type is bare soil.

Previous studies have found that the moisture contents of snow will affect the ability of electromagnetic waves to penetrate snow [34], therefore, only the case of dry snow is considered. For dry snow, the primary scattering components are the volume scattering from the snow layer and the surface scattering from the snow-ground interface. The intensity of these two primary scattering components from dry snow is dependent on the wavelength [35], [36]. The longer the wavelength is, the stronger the surface scattering from the snow-ground interface is.

B. Improved Methods for Extracting Parameters of the DM-RVoG Model

The φ_{g} and the $\gamma_{\mathrm{vol\_op}}$ are two important input parameters when using the DM-RVoG model to retrieve SD. Traditionally, these parameters have been represented using approximations of single or combined polarization channels, but the error of parameter extraction may cause greater retrieval error for targets with small thicknesses, such as snow. In this section, by considering the components and types of backscattering from snow, we propose to use the polarization decomposition method to extract φ_{g} and the coherence region boundary estimation method to extract $\gamma_{\mathrm{vol\_op}}$.

1) Polarization Decomposition for Obtaining φ_g: Freeman-Durden decomposition is a common three-component polarization decomposition method originally used for PolSAR data [37]. It is a widely utilized approach in vegetation research that extracts the contribution of three scattering components solely based on the physical characteristics of the scatterer, without reliance on measured data [37]. As analyzed in Section III-A, this decomposition method can theoretically be used to decompose snow. Recently, relevant research has demonstrated that the Freeman-Durden decomposition has a good effect on snow and ice [34], [38]. In addition, the application of the Freeman-Durden decomposition to PolInSAR is an alluring idea, which can obtain the energy contributions and the scattering phase centers of different scattering types [39]. Fig. 7 shows the decomposition of various scattering types from dry snow. From Fig. 7, the scattering process of dry snow whose underlying surface of snow cover is bare soil can be decomposed into surface scattering from the snow-ground interface and volume scattering from the snow layer.

Applied Freeman-Durden decomposition method in PolInSAR mainly constructs the undetermined equation by the polarization cross-covariance matrix ($\mathbf{C_{int}}$) [39]. $\mathbf{C_{int}}$ can be obtained by calculating the conjugate transposition of the outer positive of the target scattering vector (1) corresponding to the Lexicographic basis, as shown in the following:

$$\begin{aligned}\boldsymbol{k_{L1}} &= [S_{HH1}, S_{HV1}, S_{VH1}, S_{VV1}]^T \\ \boldsymbol{k_{L2}} &= [S_{HH2}, S_{HV2}, S_{VH1}, S_{VV2}]^T \end{aligned} \tag{1}$$

$$\begin{aligned}\boldsymbol{C_{\mathbf{int}}} &= \begin{vmatrix} \mathrm{C}_{11} & \mathrm{C}_{12} & \mathrm{C}_{13} \\ \mathrm{C}_{21} & \mathrm{C}_{22} & \mathrm{C}_{23} \\ \mathrm{C}_{31} & \mathrm{C}_{32} & \mathrm{C}_{33} \end{vmatrix} \\ &= \begin{vmatrix} \langle S_{vv1} S_{vv2}^* \rangle & \langle \sqrt{2} S_{vv1} S_{vh2}^* \rangle & \langle S_{vv1} S_{hh2}^* \rangle \\ \langle \sqrt{2} S_{vh1} S_{vv2}^* \rangle & \langle 2 S_{vh1} S_{vh2}^* \rangle & \langle \sqrt{2} S_{vh1} S_{hh2}^* \rangle \\ \langle S_{hh1} S_{vv2}^* \rangle & \langle \sqrt{2} S_{hh1} S_{vh2}^* \rangle & \langle S_{hh1} S_{hh2}^* \rangle \end{vmatrix} \end{aligned} \tag{2}$$

where $<\bullet>$ represents the mean filtering.

Second, the $\mathbf{C_{int}}$ can be decomposed into matrices of different scattering types, as shown in (3), where $\mathbf{C_{suf}}$ is the scattering matrix of surface scattering, $\mathbf{C_{vol}}$ is the scattering matrix of volume scattering, and $\mathbf{C_{dou}}$ is the scattering matrix of double-bounce scattering

$$\begin{aligned}\mathbf{C_{int}} &= \begin{vmatrix} \mathrm{C}_{11} & \mathrm{C}_{12} & \mathrm{C}_{13} \\ \mathrm{C}_{21} & \mathrm{C}_{22} & \mathrm{C}_{23} \\ \mathrm{C}_{31} & \mathrm{C}_{32} & \mathrm{C}_{33} \end{vmatrix} = \mathbf{C_{suf}} + \mathbf{C_{vol}} + \mathbf{C_{dou}} \\ &= \begin{vmatrix} F_v + F_d + F_s & 0 & \alpha F_d + \beta F_s + \frac{F_v}{3} \\ 0 & \frac{F_v}{3} & 0 \\ \alpha^* F_d + \beta^* F_s + \frac{F_v}{3} & 0 & |\alpha|^2 F_d + |\beta|^2 F_s + F_v \end{vmatrix} \end{aligned} \tag{3}$$

where F_s, F_d, and F_v are the surface, double-bounce, and volume scattering contributions, as shown in (4), (5), and (6), respectively. α and β are the Fresnel and Bragg coefficients, respectively

$$F_s = |\mathrm{Svv1}|^2 e^{j\Delta_p^s} \tag{4}$$

$$F_v = \frac{3\pi}{4} e^{j\Delta_p^v} \tag{5}$$

$$F_d = |R_{gv} R_{tv}|^2 e^{j\Delta_p^d} \tag{6}$$

where $e^{j\Delta_p^s}$, $e^{j\Delta_p^v}$, and $e^{j\Delta_p^d}$ are the surface scattering phase, the volume scattering phase, and the double-bounce scattering phase, respectively. R_{gv}, R_{tv}, R_{gh}, and R_{th} are the Fresnel coefficients, which need to be considered when the underlying surface type is vegetation [39].

The F_v and the $e^{j\Delta_p^v}$ can be directly calculated from (3). The remainder in (3) is an indeterminate system consisting of three equations and four unknowns. In this study, the indeterminate system is solved by the nonlinear least square method. Through solution, $e^{j\Delta_p^s}$ representing the φ_g can be obtained.

2) Optimizing γ_{vol_op} by Coherence Region Boundary Estimation Method: The height of the target is correlated with the volume scattering [11]. In the past, the HV polarization channel was usually considered as pure volume scattering component, that is, the ground-to-volume power ratio in the HV polarization channel was zero [40]. However, there are some ground scattering components in the HV polarization channel [37], making it inaccurate to represent the volume scattering. In this study, we used the coherence region boundary estimation method to extract the $\gamma_{\mathrm{vol\_op}}$. As shown in Fig. 8, the complex coherence of different polarization channels can be fitted with a line representing the coherence region. This line intersects with the complex unit circle at two points. The first point, labeled as the ground phase point (yellow), is far from the complex coherence of the HV polarization channel (red). The second intersection point is considered as the error solution (white). There is a fuzzy region (dashed line) between the white point and red point, and the points in this fuzzy region are more representative of pure volume scattering. This means that the boundary points of the dashed line need to be found to represent the $\gamma_{\mathrm{vol\_op}}$. The problem of determining the boundary in this dashed line can be resolved by finding the eigenvector that corresponds to the $\gamma_{\mathrm{vol\_op}}$.

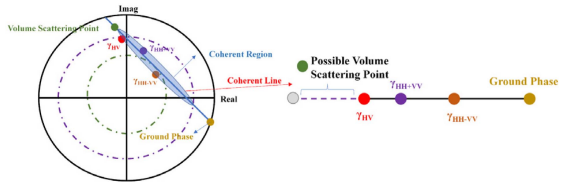

Fig. 8. Schematic diagram depicting the methodology for estimating the boundary of the coherence region.

The core step of optimizing $\gamma_{\mathrm{vol\_op}}$ is to calculate its corresponding eigenvector. First, to calculate the complex coherence of different polarization combinations, it is necessary to calculate the polarization coherence matrix ($\mathbf{T}$) and polarization interference matrix (Ω). In the case that the scattering process satisfies mutuality, calculate the outer product of the target scattering vector ($\mathbf{k_6}$) and its conjugate transpose, and obtain a 6∗6 Pauli coherence matrix ($\mathbf{T_6}$)

$$\mathbf{k_1} = \frac{1}{\sqrt{2}} [\mathrm{S_{HH1}} + \mathrm{S_{VV1}}\ \mathrm{S_{HH1}} - \mathrm{S_{VV1}}\ 2\mathrm{S_{HV1}}]^{\mathrm{T}} \tag{7}$$

$$\mathbf{k_2} = \frac{1}{\sqrt{2}} [\mathrm{S_{HH2}} + \mathrm{S_{VV2}}\ \mathrm{S_{HH2}} - \mathrm{S_{VV2}}\ 2\mathrm{S_{HV2}}]^{\mathrm{T}}$$

$$\mathbf{k_6} = [\mathbf{k_1}\ \mathbf{k_2}]^{\mathrm{T}} \tag{8}$$

$$\begin{aligned}\mathbf{T_6} &= \langle \mathbf{k_6} \bullet \mathbf{k_6^H} \rangle = \begin{bmatrix} \langle \mathbf{k_1} \bullet \mathbf{k_1^H} \rangle & \langle \mathbf{k_1} \bullet \mathbf{k_2^H} \rangle \\ \langle \mathbf{k_2} \bullet \mathbf{k_1^H} \rangle & \langle \mathbf{k_2} \bullet \mathbf{k_2^H} \rangle \end{bmatrix} \\ &= \begin{bmatrix} \mathbf{T_{11}} & \mathbf{\Omega_{12}} \\ \mathbf{\Omega_{12}^H} & \mathbf{T_{22}} \end{bmatrix} \end{aligned} \tag{9}$$

where $\mathbf{T_{11}}$ and $\mathbf{T_{22}}$ are as shown in (10) at the bottom of the next page, and Ω_{12} is as shown in (11) at the bottom of the next page.

Then, the coherence coefficients for the different polarization combinations can be obtained in the following:

$$\gamma\ (\boldsymbol{\omega}_1, \boldsymbol{\omega}_2) = \frac{\langle \mathrm{I_1 I_2^*} \rangle}{\sqrt{\langle \mathrm{I_1 I_1^*} \rangle \langle \mathrm{I_2 I_2^*} \rangle}} = \frac{\boldsymbol{\omega}_1^H \mathbf{\Omega_{12}} \boldsymbol{\omega}_2}{\sqrt{\left(\boldsymbol{\omega}_1^{\mathrm{H}} \mathbf{T_{11}} \boldsymbol{\omega}_2\right)\left(\boldsymbol{\omega}_1^{\mathrm{H}} \mathbf{T_{22}} \boldsymbol{\omega}_2\right)}} \tag{12}$$

where ω is the eigenvector of different scattering types. In practical applications, $\mathbf{T_{11}} = \mathbf{T_{22}}$ [41], hence (12) can be simplified to the following:

$$\gamma(\boldsymbol{\omega_1}, \boldsymbol{\omega_2}) = \frac{\boldsymbol{\omega_1}^{\mathrm{H}} \boldsymbol{\Omega_{12}}\, \boldsymbol{\omega_2}}{(\boldsymbol{\omega_1}^{\mathrm{H}} \mathbf{T}\, \boldsymbol{\omega_2})} \tag{13}$$

where $\mathbf{T} = (\mathbf{T_{11}}+\mathbf{T_{22}})/2$. Since $2\sqrt{(\boldsymbol{\omega_1}^{\mathrm{H}}\mathbf{T_{11}}\boldsymbol{\omega_2})(\boldsymbol{\omega_1}^{\mathrm{H}}\mathbf{T_{22}}\boldsymbol{\omega_2})} \le (\boldsymbol{\omega_1}^{\mathrm{H}}\mathbf{T_{11}}\boldsymbol{\omega_2}) + (\boldsymbol{\omega_1}^{\mathrm{H}}\mathbf{T_{22}}\boldsymbol{\omega_2})$, therefore, $|\bar{\gamma}| \le |\gamma|$ and $\arg(\gamma) = \arg(\bar{\gamma})$, then according to (18) and after the ground phase bias, we can obtain the following:

$$\begin{aligned} \mathrm{Re}\left(\tilde{\gamma}\exp\left(j\varphi_g\right)\right) &= \frac{\boldsymbol{\omega}^H((e^{j\varphi_g}\boldsymbol{\Omega}_{12}+e^{-j\varphi_g}\boldsymbol{\Omega}_{12}^H)/2)\boldsymbol{\omega}}{\boldsymbol{\omega}^H\boldsymbol{T}\boldsymbol{\omega}} \\ \text{where, } \boldsymbol{A} &= (e^{j\varphi_g}\boldsymbol{\Omega}_{12} + e^{-j\varphi_g}\boldsymbol{\Omega}_{12}^H)/2. \end{aligned} \tag{14}$$

The complex Lagrangian function is (15) by using the maximization method:

$$L = \boldsymbol{\omega}^{\mathrm{H}}\mathbf{A}\omega + \lambda(\boldsymbol{\omega}^{\mathrm{H}}\mathbf{T}\boldsymbol{\omega} - \mathrm{C}_1). \tag{15}$$

At this time, the extreme value problem can be converted into a generalized eigenvalue problem of the matrix. When calculating the extreme value, $\frac{\partial L}{\partial \boldsymbol{\omega}^H} = 0$, thus

$$\mathbf{A}\omega = \lambda\mathbf{T}\omega. \tag{16}$$

By solving (16), two possible pure $\gamma_{\mathrm{vol\_op}}$ (γ_1 and γ_2) can be computed by the following:

$$\gamma_1 = \frac{\boldsymbol{\omega_1}^{\mathrm{H}}\boldsymbol{\Omega_{12}}\boldsymbol{\omega_1}}{(\boldsymbol{\omega_1}^{\mathrm{H}}\mathbf{T}\,\boldsymbol{\omega_1})} \tag{17}$$

$$\gamma_2 = \frac{\boldsymbol{\omega_2}^{\mathrm{H}}\boldsymbol{\Omega_{12}}\boldsymbol{\omega_2}}{(\boldsymbol{\omega_2}^{\mathrm{H}}\mathbf{T}\,\boldsymbol{\omega_2})}. \tag{18}$$

Finally, using the φ_{g}, it can be determined which of γ_1 and γ_2 is the point farthest from the ground. The farthest points can represent pure $\gamma_{\mathrm{vol\_op}}$, as shown in the following:

$$\gamma_{\mathrm{vol\_op}} = \begin{cases} \gamma_1, \ if \ \ |\gamma_1 - \exp(-j\varphi_g)| > |\gamma_2 - \exp(-j\varphi_g)| \\ \gamma_2, \ if \ \ |\gamma_1 - \exp(-j\varphi_g)| < |\gamma_2 - \exp(-j\varphi_g)|. \end{cases} \tag{19}$$

C. Strategy of the DM-RVoG Model for Retrieving SD

The RVoG model considers the backscattering process as volume backscattering and ground backscattering, and was originally developed to retrieve the height of sparse medium [42], [43], such as vegetation. According to Section III-A, although dry snow is also a typical combination of these two backscattering, the RVoG model cannot be used directly because of the dense medium property of snow. From Fig. 9, when the target has

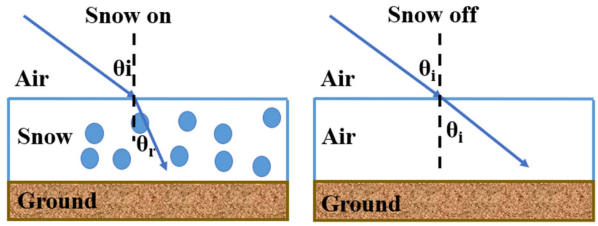

Fig. 9. Path of EW when propagating in dense medium and air. (a) Path of EW when propagating in dense medium. (b) Path of EW when propagating in air.

dense medium property, the electromagnetic wave (EW) will be refracted, and when the target is air, there will be no refraction. After considering this factor, a two-layer RVoG model suitable for dense medium such as snow and ice was derived [18], [44].

For a two-layer dense random scatterer (e.g., snow) whose volume scattering model has a limited vertical distribution and is affected by volume decorrelation, its complex correlation can be given by the following [18], [44]:

$$\gamma = \gamma_{\mathrm{SNR}} \cdot \gamma_g \cdot \gamma_{\mathrm{InSAR}} \tag{20}$$

where γ_{SNR} and γ_{g} are the noises caused by thermal noise and baseline geometry, respectively, which can be classified as system noise. The remaining part in (20) is the InSAR decorrelation (γ_{InSAR}), as in the following:

$$\gamma_{\mathrm{InSAR}} = e^{j\varphi_g}\frac{\gamma_{\mathrm{vol}} + m}{1+m} \tag{21}$$

$$\text{where, } e^{j\varphi_g}\gamma_{\mathrm{vol}} = \left|\frac{pe^{(\mathrm{P}_1\cdot\mathrm{SD})}-1}{p_1 e^{(\mathrm{P}_1\cdot\mathrm{SD})}-1}\right|, \ \text{where} \begin{cases} p = \frac{2\sigma}{\cos\theta_r} \\ p_1 = p + ikz_{\mathrm{DM}} \end{cases}. \tag{22}$$

γ_{vol} is the volume decorrelation, θ_r is the refraction angle, σ is the extinction coefficient, SD is the snow depth, kz_{DM} is the dense medium vertical wavenumber as shown in (23), m is the ground and volume power ratio, and $m = 0$ when only volume scattering is included

$$kz_{\mathrm{DM}} = \frac{n\cos\theta_r}{\cos\theta_i}kz \tag{23}$$

where n is the refractive index, θ_i is the incident angle, and kz is the vertical wavenumber calculated in free space.

A look-up table between volume decorrelation and SD is constructed according to (22) using a three-stage algorithm [24]. Then, retrieve the look-up table by the method shown in (24) to

$$\langle \mathbf{T_{ii}} \rangle = \frac{1}{2}\begin{bmatrix} \left\langle |\mathrm{S_{HH_i}} + \mathrm{S_{VV_i}}|^2 \right\rangle & \langle (\mathrm{S_{HH_i}} + \mathrm{S_{VV_i}})(\mathrm{S_{HH_i}} - \mathrm{S_{VV_i}})^* \rangle & 2\langle (\mathrm{S_{HH_i}} + \mathrm{S_{VV_i}})\mathrm{S}^*_{\mathrm{HV_i}} \rangle \\ \langle (\mathrm{S_{HH_i}} - \mathrm{S_{VV_i}})(\mathrm{S_{HH_i}} + \mathrm{S_{VV_i}})^* \rangle & \left\langle |\mathrm{S_{HH_i}} - \mathrm{S_{VV_i}}|^2 \right\rangle & 2\langle (\mathrm{S_{HH_i}} - \mathrm{S_{VV_i}})\mathrm{S}^*_{\mathrm{HV_i}} \rangle \\ 2\langle \mathrm{S_{HV_i}}(\mathrm{S_{HH_i}} + \mathrm{S_{VV_i}})^* \rangle & 2\langle \mathrm{S_{HV_i}}(\mathrm{S_{HH_i}} - \mathrm{S_{VV_i}})^* \rangle & 4\left\langle |\mathrm{S_{HV_i}}|^2 \right\rangle \end{bmatrix} \tag{10}$$

$$\boldsymbol{\Omega_{12}} = \frac{1}{2}\begin{bmatrix} \langle (\mathrm{S_{HH_1}} + \mathrm{S_{VV_1}})(\mathrm{S_{HH_2}} + \mathrm{S_{VV_2}})^* \rangle & \langle (\mathrm{S_{HH_1}} + \mathrm{S_{VV_1}})(\mathrm{S_{HH_2}} - \mathrm{S_{VV_2}})^* \rangle & 2\langle (\mathrm{S_{HH_1}} + \mathrm{S_{VV_1}})\mathrm{S}^*_{\mathrm{HV_2}} \rangle \\ \langle (\mathrm{S_{HH_1}} - \mathrm{S_{VV_1}})(\mathrm{S_{HH_2}} + \mathrm{S_{VV_2}})^* \rangle & \langle (\mathrm{S_{HH_1}} - \mathrm{S_{VV_1}})(\mathrm{S_{HH_2}} - \mathrm{S_{VV_2}})^* \rangle & 2\langle (\mathrm{S_{HH_1}} - \mathrm{S_{VV_1}})\mathrm{S}^*_{\mathrm{HV_2}} \rangle \\ 2\langle \mathrm{S_{HV_1}}(\mathrm{S_{HH_2}} + \mathrm{S_{VV_2}})^* \rangle & 2\langle \mathrm{S_{HV_1}}(\mathrm{S_{HH_2}} - \mathrm{S_{VV_2}})^* \rangle & 4\langle (\mathrm{S_{HV_1}})(\mathrm{S_{HV_2}})^* \rangle \end{bmatrix}. \tag{11}$$

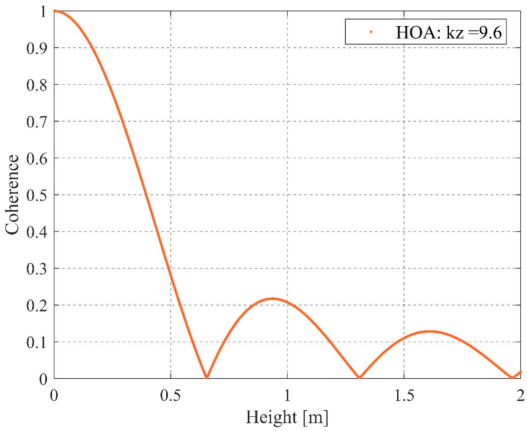

Fig. 10. Corresponding HOA of the SAR data pair. The figure displays the lookup table of the three-stage algorithm computed from the experimental SAR data.

obtain the corresponding SD

$$\min_D \ (\mathrm{SD},\ \sigma) = \left\| \gamma_{\mathrm{vol\_op}} \ - \ e^{j\varphi_g} \gamma_{\mathrm{vol}} \right\| \tag{24}$$

where the φ_g and $\gamma_{\mathrm{vol\_op}}$ can be calculated by the method proposed in Section III-B.

D. Implementation of the Proposed Method

The core process of the novel method to retrieve SD is DM-RVoG model, and the parameters involved mainly include the φ_g, $\gamma_{\mathrm{vol\_op}}$, σ, and kz_{DM}, where the φ_g and $\gamma_{\mathrm{vol\_op}}$ can be extracted by Section III-B. For the extinction coefficient, the initial value of the extinction coefficient needs to be determined when using the three-stage algorithm. In previous studies, we obtained the σ of the snowpack in the study area for different periods through long-term field observations [45]. In this study, the average extinction coefficient of 1.5 was used as the overall snow extinction coefficient. In the absence of ground measurements, the extinction coefficient can also be estimated from the incident angle, the dielectric constant, and the snow density [11]. For dense medium vertical wavenumber, this parameter will determine the height range (HOA) that the DM-RVoG model can retrieve. The calculated results shown in Fig. 10 indicate that the maximum SD that can be retrieved by the DM-RVoG model is 67.5 cm, which can achieve the snow situation. The proposed method can be implemented after obtaining the above parameters.

E. Metrics for Accuracy Assessment

In this study, the precision is evaluated by utilizing measured SD points. Typically, the accuracy assessment metrics used include the correlation coefficient (R), root-mean-square error (RMSE), and average absolute error (MAE) [46]. R represents the correlation between the remote sensing retrieval value and the measurement value, as shown in (25). RMSE and MAE can measure the specific difference between the remote sensing retrieval value and the in situ measurement value, as shown in (26) and (27). Compared with RMSE, MAE is less susceptible to outliers and generally regarded as more reliable than RMSE

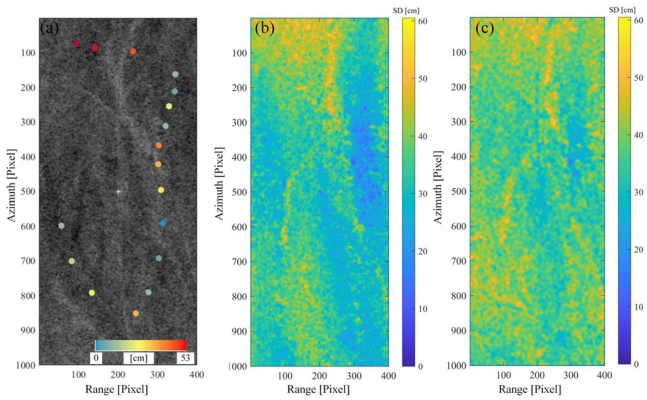

Fig. 11. SD retrieval results. (a) Is the SAR map with the measured SD. (b) and (c) are the SD obtained by the novel and original methods.

$$R = \frac{\mathrm{Cov}\left(\mathrm{RS}_i,\ \ \mathrm{AM}_i\right)}{\sqrt{\mathrm{var}\left(\mathrm{RS}_i\right)\mathrm{var}\left(\mathrm{AM}_i\right)}} \tag{25}$$

$$\mathrm{RMSE} = \sqrt{\frac{1}{n}\sum_{i=1}^{n}\left(\mathrm{RS}_i - \mathrm{AM}_i\right)^2} \tag{26}$$

$$\mathrm{MAE} = \frac{\sum_{i=1}^{n}\left|\mathrm{RS}_i - \ \mathrm{AM}_i\right|}{n}. \tag{27}$$

Among them, RS_i is the retrieval SD, and AM_i is the in situ measurement SD.

IV. Results

In this section, the SD retrieval results are presented and the accuracy is assessed using in situ data. First, we show and compare the retrieved SD. Then, we assess the precision of the novel method and contrast it with the original method.

A. SD Retrieval Results

Fig. 11 presents the results of SD retrieval, including the SAR image with the measured SD and the SD retrieved by the novel and original methods. In Fig. 11, the SD obtained from the original method is thicker, which is caused by the underestimation of $\gamma_{\mathrm{vol\_op}}$ by the original method due to some ground scattering components mixed in the HV polarization channel. The variation of the SD obtained by the two methods is relatively flat. Compared with the measured SD, we found that the results of the proposed method are closer to the measured values, indicating that the proposed method is more reliable.

Fig. 12 shows the histograms of retrieval SD by the novel and original methods. The red dashed line in Fig. 12 shows the measured average SD of 20 cm. The SD obtained from the original method is concentrated at 35 cm, and the SD obtained from the novel method is concentrated at 26 cm. The SD obtained from the proposed method was found to be more accurate than the average measured SD, highlighting the accuracy of the parameters will seriously affect the accuracy of the DM-RVoG model.

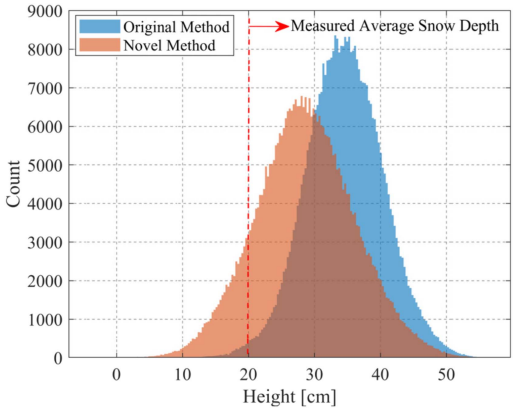

Fig. 12. Histogram of SD retrieval results. The orange part is the histogram of the novel method. The blue part is the histogram of the original method. The red dotted line is the average measured SD.

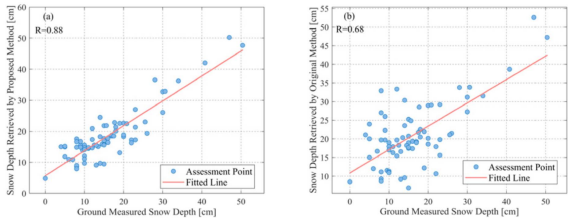

Fig. 13. Comparison between the retrieved and measured SD. (a) and (b) are the comparisons between the results of the novel and original methods and the measured values.

TABLE II
ACCURACY EVALUATION RESULTS OF TWO METHODS

Method	R	RMSE (cm)	MAE (cm)
Original Method	0.68	8.60	6.80
Proposed Method	0.88	4.92	4.08

B. Accuracy Assessment and Comparison

The in situ measured SD points were used to assess the accuracy of the novel and original methods. The retrieved and measured SD are compared in Fig. 13. There is a stronger positive correlation with an R of 0.88, which obviously improves the interpretability of the DM-RVoG model. The SD retrieval precision of the two methods was quantitatively assessed using RMSE and MAE.

The evaluation results for both methods are displayed in Table II. The *R*, RMSE, and MAE of the novel method are 0.88, 4.92 cm, and 4.08 cm, respectively. A considerable improvement in precision is observed in comparison with the original method, and the RMSE and MAE of the novel method are reduced by 3.68 and 2.72 cm, respectively. Fig. 14 is the error histogram of the two methods, which shows the bias difference between the retrieved and measured SD. The error of the novel method is basically below 10 cm in Fig. 14(a), and there is no obvious concentration error, but the retrieval error ratio is a little higher in some shallow snow positions. The main reason is that the total backscattering information from shallow snow has more backscattering components from the ground than that of deep snow, which affects the accuracy. The error of the original method is primarily overestimation, and there is even an overestimation of up to 20 cm, which is caused by the inaccurate parameter calculation.

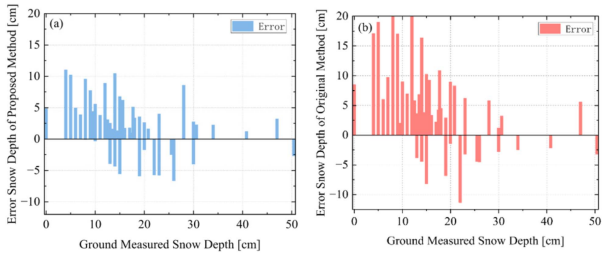

Fig. 14. Error histogram of the method before and after the improvement. (a) and (b) are the error histograms of the two methods.

V. DISCUSSION

In this study, a method to retrieve SD in response to the inaccuracy of the input parameters in the original DM-RVoG model was proposed. Through the above comparison and accuracy assessment of the proposed and original methods, we found that the precision of the proposed method in retrieving SD has been significantly improved. At the same time, we also found some factors and limitations that influence the retrieval precision of the novel method, which are discussed below.

First, the baseline between SAR data pairs is a main factor affecting the proposed method. The baseline between SAR data pairs is related to the dense medium vertical wavenumber, which can affect the maximum SD that can be retrieved by the DM-RVoG model. This is a limitation inherent in the RVoG model, and in forest and glacier applications, the error caused by the baseline is usually acceptable due to the tall targets. However, the thickness of snow is relatively small in comparison. Therefore, it is necessary to consider this factor when retrieving the SD, and choose an appropriate baseline based on the snow situations in the study area. For SAR data with controllable flight parameters, a lookup table is first constructed by (24), and then a suitable flight baseline is calculated based on the dense medium wavenumber used in the construction of the lookup table. For SAR data acquired by fixed orbit flight, the dense medium wavenumber is first calculated based on the flight baseline, and then a look-up table is constructed to determine whether the novel method can satisfy the situation of SD.

In addition, the filter window selected when estimating $\gamma_{\mathrm{vol\_op}}$ and SD is also a crucial factor affecting the SD retrieved by the proposed method. We found in experiments that too large a filter window used in estimating decorrelation and SD will cause detailed information loss, but too small a filter window increases noise. Therefore, it is necessary to combine the SAR data used for multiple experiments to select the appropriate filter window when retrieving SD. In this study, a 5∗5 average filter window is used to filter the spatio-temporal elements, which not only retains the detailed information but also filters the speckle noise.

Finally, the parameters representing the ground scattering phase center may need to be adjusted according to the different

land cover types. In Section II, we analyze the backscattering mechanisms from snow. We propose the decomposed surface scattering phase center to represent the position of the snow-ground interface, and demonstrate the validity of the proposed method when the underlying surface type is bare soil. But it has been shown that when the underlying surface type is forest, the scattering type from the snow-ground interface will change to double-bounce scattering [47], which can be obtained by the method in Section III-A.1. Therefore, to obtain the phase center representing the snow-ground interface, the actual situation must be taken into account.

VI. Conclusion

In this study, we addressed the problem of inaccurate parameters in the DM-RVoG model for snow applications and proposed a novel SD retrieval method for PolInSAR. To alleviate this problem, we proposed using the polarization decomposition method for extracting the phase center of ground scattering and the coherence region boundary estimation method for extracting the volume decorrelation. The proposed method has good performance for retrieving SD.

The factors and limitations affecting the performance of the novel method for retrieving SD were discussed including the flight baseline of SAR data, the filter window, and the underlying surface type.

In conclusion, accurate SD retrieval is essential for measuring snow variability and modeling global climate. Based on the DM-RVoG model, this study improved the original method by extracting input parameters more precisely and proposed a novel SD retrieval method with better results. In future research, more work needs to be considered about not only the tests on different terrains, imaging times, and datasets, but also the impact of snow stratification and different land cover types.

Acknowledgment

The authors would like to thank Google Earth for providing the high-resolution satellite images.

References

[1] T. V. Callaghan et al., "Multiple effects of changes in Arctic snow cover," *Ambio*, vol. 40, no. 1, pp. 32–45, 2011.
[2] R. L. Armstrong and E. Brun, *Snow and Climate: Physical Processes, Surface Energy Exchange and Modeling*. Cambridge, U.K. Cambridge Univ. Press, 2008.
[3] M. Beniston, F. Keller, B. Koffi, and S. Goyette, "Estimates of snow accumulation and volume in the Swiss Alps under changing climatic conditions," *Theor. Appl. Climatol.*, vol. 76, no. 3, pp. 125–140, 2003.
[4] S. Awasthi et al., "Snow depth retrieval in North-Western Himalayan region using pursuit-monostatic TanDEM-X datasets applying polarimetric synthetic aperture radar interferometry based inversion Modelling," *Int. J. Remote Sens.*, vol. 42, no. 8, pp. 2872–2897, Apr. 2021.
[5] Y. Bühler et al., "Snow depth mapping in high-alpine catchments using digital photogrammetry," *Cryosphere*, vol. 9, no. 1, pp. 229–243, 2015.
[6] Y.-L. S. Tsai, A. Dietz, N. Oppelt, and C. Kuenzer, "Remote sensing of snow cover using spaceborne SAR: A review," *Remote Sens.-Basel*, vol. 11, no. 12, 2019, Art. no. 1456.
[7] D. Hall, *Remote Sensing of Ice and Snow*. Berlin, Germany: Springer-Verlag, 2012.
[8] J. Shi and J. Dozier, "Estimation of snow water equivalence using SIR-C/X-SAR. II. Inferring snow depth and particle size," *IEEE Trans. Geosci. Remote Sens.*, vol. 38, no. 6, pp. 2475–2488, Nov. 2000.
[9] S. Leinss, G. Parrella, and I. Hajnsek, "Snow height determination by polarimetric phase differences in X-band SAR data," *IEEE J. Sel. Topics Appl. Earth Observ. Remote Sens.*, vol. 7, no. 9, pp. 3794–3810, Sep. 2014.
[10] F. Argenti, A. Lapini, L. Alparone, and T. Bianchi, "A tutorial on speckle reduction in synthetic aperture radar images," *IEEE Geosci. Remote Sens. Mag.*, vol. 1, no. 3, pp. 6–35, Sep. 2013.
[11] A. Patil, G. Singh, C. Rüdiger, S. Mohanty, S. Kumar, and Snehmani, "A novel approach for the snow water equivalent retrieval using X-band polarimetric synthetic aperture radar data," *IEEE Trans. Geosci. Remote Sens.*, vol. 59, no. 5, pp. 3753–3763, May 2021.
[12] G. Singh et al., "Retrieval of spatial and temporal variability in snowpack depth over glaciers in Svalbard using GPR and spaceborne POLSAR measurements," *Water*, vol. 12, no. 1, 2019, Art. no. 21.
[13] J. Voglimacci-Stephanopoli et al., "Potential of X-band polarimetric synthetic aperture radar co-polar phase difference for arctic snow depth estimation," *Cryosphere*, vol. 16, no. 6, pp. 2163–2181, 2022.
[14] J. Shi and J. Dozier, "Estimation of snow water equivalence using SIR-C/X-SAR, part I: Inferring snow density and subsurface properties," *IEEE Trans. Geosci. Remote Sens.*, vol. 38, no. 6, pp. 2465–2474, Nov. 2000.
[15] P. K. Thakur et al., "Snow physical parameters estimation using space-based synthetic aperture radar," *Geocarto Int.*, vol. 27, no. 3, pp. 263–288, 2012.
[16] M. Li, P. Xiao, X. Zhang, X. Feng, and L. Zhu, "An improved approach of dry snow density estimation using C-band synthetic aperture radar data," *ISPRS J. Photogrammetry Remote Sens.*, vol. 191, pp. 49–67, 2022.
[17] T. Guneriussen, K. A. Hogda, H. Johnsen, and I. Lauknes, "InSAR for estimation of changes in snow water equivalent of dry snow," *IEEE Trans. Geosci. Remote Sens.*, vol. 39, no. 10, pp. 2101–2108, Oct. 2001.
[18] Y. Lei et al., "Dry snow parameter retrieval with ground-based single-pass synthetic aperture radar interferometry," *IEEE Trans. Geosci. Remote Sens.*, vol. 60, 2022, Art. no. 4304614.
[19] S. Leinss, O. Antropov, J. Vehviläinen, J. Lemmetyinen, I. Hajnsek, and J. Praks, "Wet snow depth from TanDEM-X single-pass InSAR DEM differencing," in *Proc. IEEE Int. Geosci. Remote Sens. Symp.*, 2018, pp. 8500–8503.
[20] Y. Liu, L. H. Li, J. M. Yang, X. Chen, and J. S. Hao, "Estimating snow depth using multi-source data fusion based on the D-InSAR method and 3DVAR fusion algorithm," *Remote Sens.-Basel*, vol. 9, no. 11, Nov. 2017, Art. no. 1195.
[21] J. M. Yang and C. Z. Li, "Assimilation of D-InSAR snow depth data by an ensemble Kalman filter," *Arabian J. Geosci.*, vol. 14, no. 6, pp. 1–14, Mar. 2021.
[22] D. Varade, A. K. Maurya, O. Dikshit, G. Singh, and S. Manickam, "Snow depth in Dhundi: An estimate based on weighted bias corrected differential phase observations of dual polarimetric bi-temporal Sentinel-1 data," *Int. J. Remote Sens.*, vol. 41, no. 8, pp. 3031–3053, 2020.
[23] S. R. Cloude and K. P. Papathanassiou, "Polarimetric SAR interferometry," *IEEE Trans. Geosci. Remote Sens.*, vol. 36, no. 5, pp. 1551–1565, Sep. 1998.
[24] S. R. Cloude and K. P. Papathanassiou, "Three-stage inversion process for polarimetric SAR interferometry," *IEEE Proc.-Radar Sonar Navigation*, vol. 150, no. 3, pp. 125–134, Jun. 2003.
[25] J. J. Sharma, I. Hajnsek, and K. P. Papathanassiou, "Multi-frequency PolInSAR signatures of a subpolar glacier," in *Proc. 3rd Int. Workshop Sci. Appl. SAR Polarimetry Polarimetric Interferometry*, Frascati, Italy, Jan. 22-26, 2007.
[26] A. Patil, S. Mohanty, and G. Singh, "Snow depth and snow water equivalent retrieval using X-band PolInSAR data," *Remote Sens. Lett.*, vol. 11, no. 9, pp. 817–826, Sep. 2020.
[27] S. Majumdar, P. K. Thakur, L. Chang, S. Mani, and S. Kumar, "Snow depth and snow water equivalent estimation in the northwestern himalayan watershed using spaceborne polarimetric SAR Interferometry," 2020. [Online]. Available: https://doi.org/10.31223/osf.io/6v4h3
[28] Y. Zhuo, "Inversion of dry snow depth in typical Altay area based on SAR co-polar phase difference," M.S. thesis, Nanjing Univ., Nanjing, China, 2018.
[29] H. Qiao et al., "Snow profile reconstruction from tomographic UAV SAR," *Int. J. Appl. Earth Observ. Geoinf.*, vol. 118, 2023, Art. no. 103291.
[30] D. Li and Y. Zhang, "A fast offset estimation approach for InSAR image subpixel registration," *IEEE Geosci. Remote Sens. Lett.*, vol. 9, no. 2, pp. 267–271, Mar. 2012.
[31] C. T. Allen, "Interferometric synthetic aperture radar," *IEEE Geosci. Remote Sens. Soc. Newslett.*, vol. 96, pp. 6–13, 1995.
[32] J. Liu and W. Hong, "Reverse-range-doppler method for automated geocoding SAR images," *J. Electron.*, vol. 29, no. 3/4, pp. 242–247, 2012.

[33] F. T. Ulaby, W. H. Stiles, and M. A. Razik, "Snowcover influence on backscattering from terrain," *IEEE Trans. Geosci. Remote Sens.*, vol. GE-22, no. 2, pp. 126–133, Mar. 1984.
[34] Y. K. Antropova, A. S. Komarov, M. Richardson, K. Millard, and K. Smith, "Detection of wet snow in the Arctic tundra from time-series fully-polarimetric RADARSAT-2 images," *Remote Sens. Environ.*, vol. 283, 2022, Art. no. 113305.
[35] A. Martini, L. Ferro-Famil, and E. Pottier, "Polarimetric study of scattering from dry snow cover in Alpine areas," in *Proc. IEEE Int. Geosci. Remote Sens. Symp.*, 2003, vol. 2, pp. 854–856, doi: 10.1109/IGARSS.2003.1293942.
[36] C. Xiong et al., "Time series X-and Ku-band ground-based synthetic aperture radar observation of snow-covered soil and its electromagnetic modeling," *IEEE Trans. Geosci. Remote Sens.*, vol. 60, 2022, Art. no. 2000613.
[37] A. Freeman and S. L. Durden, "A three-component scattering model for polarimetric SAR data," *IEEE Trans. Geosci. Remote Sens.*, vol. 36, no. 3, pp. 963–973, May 1998.
[38] I. Pisciottano, T. Jagdhuber, G. Parrella, and I. Hajnsek, "First analysis on snow cover change using fully polarimetric TerraSAR-X data," *Proc. IEEE*, vol. 98, no. 5, pp. 752–765, 2010.
[39] J. D. Ballester-Berman and J. M. Lopez-Sanchez, "Applying the Freeman–Durden decomposition concept to polarimetric SAR interferometry," *IEEE Trans. Geosci. Remote Sens.*, vol. 48, no. 1, pp. 466–479, Jan. 2010.
[40] H. Lievens et al., "Snow depth variability in the Northern Hemisphere mountains observed from space," *Nature Commun.*, vol. 10, Oct. 2019, Art. no. 4629.
[41] E. Colin, C. Titin-Schnaider, and W. Tabbara, "An interferometric coherence optimization method in radar polarimetry for high-resolution imagery," *IEEE Trans. Geosci. Remote Sens.*, vol. 44, no. 1, pp. 167–175, Jan. 2006.
[42] K. P. Papathanassiou and S. R. Cloude, "Single-baseline polarimetric SAR interferometry," *IEEE Trans. Geosci. Remote Sens.*, vol. 39, no. 11, pp. 2352–2363, Nov. 2001.
[43] S. R. Cloude, "Polarization coherence tomography," *Radio Sci.*, vol. 41, no. 4, pp. 1–27, Aug. 2006.
[44] Y. Lei, P. Siqueira, and R. Treuhaft, "A dense medium electromagnetic scattering model for the InSAR correlation of snow," *Radio Sci.*, vol. 51, no. 5, pp. 461–480, 2016.
[45] L. Zhixian, "Electromagnetic scattering models for InSAR correlation measurements of multi-layer snow and snow depth retrieval," Ph.D. dissertation, Univ. Chin. Acad. Sci., Beijing, China, 2019.
[46] X. Hu, X. Hao, J. Wang, G. Huang, H. Li, and Q. Yang, "Can the depth of seasonal snow be estimated from ICESat-2 products: A case investigation in Altay, Northwest China," *IEEE Geosci. Remote Sens. Lett.*, vol. 19, 2022, Art. no. 2000405.
[47] S. H. Yueh, S. J. Dinardo, A. Akgiray, R. West, D. W. Cline, and K. Elder, "Airborne Ku-band polarimetric radar remote sensing of terrestrial snow cover," *IEEE Trans. Geosci. Remote Sens.*, vol. 47, no. 10, pp. 3347–3364, Oct. 2009.

Haiwei Qiao received the B.S. degree in geographical information science from Northwest Normal University, Lanzhou, China, in 2020. He is currently working toward the Ph.D. degree in cartography and geography information system in the Key Laboratory of Digital Earth Science, Aerospace Information Research Institute, Chinese Academy of Sciences, Beijing, China.

His current research interests include SAR technology and application and snow remote sensing.

Ping Zhang received the Ph.D. degree in communication and information system from the Institute of Electronics, Chinese Academy of Sciences, Beijing, China, in 2009.

She is currently an Associate Professor with the Key Laboratory of Digital Earth Science, Aerospace Information Research Institute, Chinese Academy of Sciences. She has authored and coauthored more than 20 articles and three book chapters. Her current research interests include remote sensing data processing, signal processing, and calibration of SAR

Zhen Li (Member, IEEE) received the B.S. degree in photogrammetry and remote sensing from Wuhan University, Wuhan, China, in 1988, and the Ph.D. degree in natural geography from the Cold and Arid Regions Environmental and Engineering Research Institute, Chinese Academy of Sciences, Lanzhou, China, in 1998.

He is currently a Professor with the Key Laboratory of Digital Earth Science, Aerospace Information Research Institute, Chinese Academy of Sciences, Beijing, China. He has authored more than 100 journal papers and has authored and coauthored four books in collaboration with others. His current research interests include microwave remote sensing, cryosphere environment, and disaster remote sensing.

Lei Huang (Member, IEEE) received the Ph.D. degree in cartography and geographical information system from the Institute of Remote Sensing and Digital Earth, Chinese Academy of Sciences, Beijing, China, in 2010.

He is currently an Associate Professor with the International Research Center of Big Data for Sustainable Development Goals, and Aerospace Information Research Institute, Chinese Academy of Sciences. His research interests include remote sensing of glacier, snow, and climate change.

Dr. Huang is a member of Youth Innovation Promotion Association of Chinese Academy of Sciences.

Zhipeng Wu received the B.S. degree in remote sensing science and technology from the China University of Geosciences, Wuhan, China, in 2019, and the M.S. degree in cartography and geographical information system from the Key Laboratory of Digital Earth Science, Aerospace Information Research Institute, Chinese Academy of Sciences, Beijing, China, in 2022.

His research interests include radar remote sensing vegetation parameter inversion and signal processing.

Shuo Gao received the B.S. degree in remote sensing science and technology from Shandong Agricultural University, Taian, China, in 2016, and the Ph.D. degree in cartography and geographical information system from the Aerospace Information Research Institute, Chinese Academy of Sciences, Beijing, China, in 2022.

He is currently an Assistant to Special Researcher with the State Key Laboratory of Remote Sensing Science, Aerospace Information Research Institute, Chinese Academy of Sciences. His current research interests include microwave modeling and retrieval methods of snow and hydrological applications of satellite remote sensing.

Chang Liu received the Ph.D. degree in cartography and geographical information system from the Key Laboratory of Digital Earth Science, Aerospace Information Research Institute, Chinese Academy of Sciences, Beijing, China, in 2022.

Her research interests include assessment and application of snow cover products, microwave remote sensing of snow parameters, and hydrological applications of satellite remote sensing.

Shuang Liang received the Ph.D. degree in cartography and geographic information system from the Aerospace Information Research Institute, Chinese Academy of Sciences, Beijing, China.

Her current and previous research interests include remote sensing of snow and ice.

Jianmin Zhou received the Ph.D. degree in cartography and geography information system from the Institute of Remote Sensing Applications, Chinese Academy of Sciences, Beijing, China, in 2009.

He is currently an Associate Professor with the Key Laboratory of Digital Earth Science, Aerospace Information Research Institute, Chinese Academy of Sciences. He has authored and coauthored more than 40 articles and three book chapters. His research interests include InSAR, cryosphere remote sensing, and environment and disaster remote sensing

Wei Sun received the M.S. degree in engineering from Beijing Jiaotong University, Beijing, China, in 2005.

He is currently an Associate Research Fellow with the National Key Laboratory of Microwave Imaging Technology, Aerospace Information Research Institute, Chinese Academy of Sciences, Beijing. His research interests include system designing of synthetic aperture radar.

Jian Wang received the M.S. degree in surveying and mapping from the Anhui University of Science and Technology, Anhui, China, in 2023.

He is currently an Assistant Engineer with the Geographic Information Monitoring Department, Zhejiang Mingzhou Institute of Surveying and Mapping, Ningbo, China. His research interests include automatic interpretation of remote sensing images and forest microwave remote sensing.